Biomedical Optics EXPRESS

Non-invasive fluorescence imaging under ambient light conditions using a modulated ICCD and laser diode

Banghe Zhu,* John C. Rasmussen, and Eva M. Sevick-Muraca

Center for Molecular Imaging, The Brown Foundation Institute of Molecular Medicine, The University of Texas Health Science Center, Houston, Texas, 77030 USA
**Banghe.Zhu@uth.tmc.edu*

Abstract: One limitation of fluorescence molecular imaging that can limit clinical implementation and hamper small animal imaging is the inability to eliminate ambient light. Herein, we demonstrate the ability to conduct rapid non-invasive, far-red and near-infrared fluorescence imaging in living animals and a phantom under ambient light conditions using a modulated image intensified CCD (ICCD) and a laser diode operated in homodyne detection. By mapping AC amplitude from three planar images at varying phase delays, we show improvement in target-to-background ratios (TBR) and reasonable signal-to-noise ratios (SNR) over continuous wave measurements. The rapid approach can be used to accurately collect fluorescence in situations where ambient light cannot be spectrally conditioned or controlled, such as in the case of fluorescent molecular image-guided surgery.

OCIS codes: (260.2510) Fluorescence; (060.2630) Frequency modulation; (040.1520) CCD, charge-coupled device.

References and links

1. B. Zhu, G. Wu, H. Robinson, N. Wilganowski, M. A. Hall, S. C. Ghosh, K. L. Pinkston, A. Azhdarinia, B. R. Harvey, and E. M. Sevick-Muraca, "Tumor Margin Detection Using Quantitative NIRF Molecular Imaging Targeting EpCAM Validated by Far Red Gene Reporter iRFP," Mol. Imaging Biol. **15**(5), 560–568 (2013).
2. B. Zhu, J. C. Rasmussen, Y. Lu, and E. M. Sevick-Muraca, "Reduction of excitation light leakage to improve near-infrared fluorescence imaging for tissue surface and deep tissue imaging," Med. Phys. **37**(11), 5961–5970 (2010).
3. B. Zhu and E. M. Sevick-Muraca, "Minimizing excitation light leakage and maximizing measurement sensitivity for molecular imaging with near-infrared fluorescence," J. Innovative Opt. Health Sci. **4**(03), 301–307 (2011).
4. A. M. De Grand and J. V. Frangioni, "An operational near-infrared fluorescence imaging system prototype for large animal surgery," Technol. Cancer Res. Treat. **2**(6), 553–562 (2003).
5. G. Themelis, J. S. Yoo, K.-S. Soh, R. Schulz, and V. Ntziachristos, "Real-time intraoperative fluorescence imaging system using light-absorption correction," J. Biomed. Opt, **14**, 064012 (2009).
6. C. H. Heath, N. L. Deep, L. N. Beck, K. E. Day, L. Sweeny, K. R. Zinn, C. C. Huang, and E. L. Rosenthal, "Use of Panitumumab-IRDye800 to Image Cutaneous Head and Neck Cancer in Mice," Otolaryngol. Head Neck Surg. **148**(6), 982–990 (2013).
7. S. Keereweer, J. D. F. Kerrebijn, P. B. A. A. van Driel, B. Xie, E. L. Kaijzel, T. J. A. Snoeks, I. Que, M. Hutteman, J. R. van der Vorst, J. S. D. Mieog, A. L. Vahrmeijer, C. J. van de Velde, R. J. Baatenburg de Jong, and C. W. Löwik, "Optical image-guided surgery--where do we stand?" Mol. Imaging Biol. **13**(2), 199–207 (2011).
8. G. M. van Dam, G. Themelis, L. M. A. Crane, N. J. Harlaar, R. G. Pleijhuis, W. Kelder, A. Sarantopoulos, J. S. de Jong, H. J. G. Arts, A. G. J. van der Zee, J. Bart, P. S. Low, and V. Ntziachristos, "Intraoperative tumor-specific fluorescence imaging in ovarian cancer by folate receptor-α targeting: first in-human results," Nat. Med. **17**(10), 1315–1319 (2011).
9. S. Keereweer, P. B. A. A. Van Driel, T. J. A. Snoeks, J. D. F. Kerrebijn, R. J. Baatenburg de Jong, A. L. Vahrmeijer, H. J. C. M. Sterenborg, and C. W. G. M. Löwik, "Optical Image-Guided Cancer Surgery: Challenges and Limitations," Clin. Cancer Res. **19**(14), 3745–3754 (2013), doi:10.1158/1078-0432.
10. K. Sexton, S. C. Davis, D. McClatchy 3rd, P. A. Valdes, S. C. Kanick, K. D. Paulsen, D. W. Roberts, and B. W. Pogue, "Pulsed-light imaging for fluorescence guided surgery under normal room lighting," Opt. Lett. **38**(17), 3249–3252 (2013).

#200854 - $15.00 USD Received 6 Nov 2013; revised 22 Jan 2014; accepted 22 Jan 2014; published 24 Jan 2014

11. C. D. Darne, Y. Lu, and E. M. Sevick-Muraca, "Small animal fluorescence and bioluminescence tomography: a review of approaches, algorithms and technology update," Phys. Med. Biol. **59**(1), R1–R64 (2014).
12. J. P. Houston, A. B. Thompson, M. Gurfinkel, and E. M. Sevick-Muraca, "Sensitivity and Depth Penetration of Continuous Wave Versus Frequency-domain Photon Migration Near-Infrared Fluorescence Contrast-Enhanced Imaging," Photochem. Photobiol. **77**(4), 420–430 (2003).
13. A. Godavarty, M. J. Eppstein, C. Zhang, S. Theru, A. B. Thompson, M. Gurfinkel, and E. M. Sevick-Muraca, "Fluorescence-enhanced optical imaging in large tissue volumes using a gain-modulated ICCD camera," Phys. Med. Biol. **48**(12), 1701–1720 (2003).
14. C. D. Darne, Y. Lu, I. C. Tan, B. Zhu, J. C. Rasmussen, A. M. Smith, S. Yan, and E. M. Sevick-Muraca, "A compact frequency-domain photon migration system for integration into commercial hybrid small animal imaging scanners for fluorescence tomography," Phys. Med. Biol. **57**(24), 8135–8152 (2012).
15. E. M. Sevick-Muraca, and J. C. Rasmussen, "Molecular imaging with optics: primer and case for near-infrared fluorescence techniques in personalized medicine," J. Biomed. Opt. **13**, 041303 (2008).
16. A. B. Thompson and E. M. Sevick-Muraca, "Near-infrared fluorescence contrast-enhanced imaging with intensified charge-coupled device homodyne detection: measurement precision and accuracy," J. Biomed. Opt. **8**(1), 111–120 (2003).
17. G. S. Filonov, K. D. Piatkevich, L.-M. Ting, J. Zhang, K. Kim, and V. V. Verkhusha, "Bright and stable near-infrared fluorescent protein for in vivo imaging," Nat. Biotechnol. **29**(8), 757–761 (2011).
18. J. P. Houston, S. Ke, W. Wang, C. Li, and E. M. Sevick-Muraca, "Quality analysis of in vivo near-infrared fluorescence and conventional gamma images acquired using a dual-labeled tumor-targeting probe," J. Biomed. Opt. **10**, 054010 (2005).
19. K. Murthy, M. Aznar, C. J. Thompson, A. Loutfi, R. Lisbona, and J. H. Gagnon, "Results of preliminary clinical trials of the positron emission mammography system PEM-I: a dedicated breast imaging system producing glucose metabolic images using FDG," J. Nucl. Med. **41**(11), 1851–1858 (2000).
20. F. Meric-Bernstam, J. C. Rasmussen, S. Krishnamurthy, I. Tan, B. Zhu, J. L. Wagner, G. V. Babiera, E. A. Mittendorf, and E. M. Sevick-Muraca, "Toward nodal staging of axillary lymph node basins through intradermal administration of fluorescent imaging agents," Biomed. Opt. Express **5**(1), 183–196 (2014).

1. Introduction

Although much progress has been made to develop new effective cancer therapeutics, surgery remains the foundation of curative treatment with optimal outcomes occurring with complete resection of primary lesions and, in the case of advanced high-risk cancer patients, for debulking (or cytoreductive surgery) prior to adjuvant radiation and/or systemic chemotherapy. In most cancers, residual tumor burden after surgical resection is correlated with poor outcome. Yet despite the importance of resecting as much cancer as possible, only tactile cues are currently used to guide resection. In the case of endoscopic or laparoscopic surgery, surgeons do not have these tactile cues. Successful image-guided surgery based upon fluorescently labeled imaging agents requires exogenous fluorescent signals from diseased tissues to be above the noise floor and to have adequate contrast relative to background, or normal tissues. Since surgical resection is most facile with fluorescence imaging concurrent with illumination that preserves the surgeon's visual acuity, it is critical to eliminate ambient light to enable high imaging contrast.

In preclinical animal studies, the advent of far-red gene reporters that can be incorporated into tumor models [1] offers powerful new opportunities to longitudinally monitor metastases. Yet for faithful detection, fluorescent signals again need to exceed the noise floor of the imaging device. As we have previously shown, the noise floor of planar fluorescent imaging devices can be reduced by minimizing leakage of out-of-band light through filters [2, 3], however, when ambient light contains "in-band" spectral components, optical filtering may not sufficiently lower the noise floor and reduced imaging sensitivity will result.

Herein, we demonstrate an electronic filtering feature than can minimize the influence of "in-band" light. Current CCD camera based fluorescence imaging systems for intraoperative image-guided tumor detection [4–9] employ continuous wave (CW) image acquisition due to its low cost and simple implementation. Recently, a fluorescence-guided system which used pulsed excitation and gated microsecond acquisition to reject ambient light through the subtraction of intensity measurements made in the absence and presence of excitation illumination termed time-domain (TD) approach demonstrated improved performance [10]. While approaches based used upon RF modulated excitation light (termed frequency-domain (FD) approaches) have been proposed and used in small animal tomography studies [11], they can also be operated in a non-light-tight environments because the AC amplitude of the

#200854 - $15.00 USD Received 6 Nov 2013; revised 22 Jan 2014; accepted 22 Jan 2014; published 24 Jan 2014

detected fluorescence is insensitive to changing ambient light conditions [12]. Previously, we coupled near-infrared sensitive Gen III image intensifiers for electronically amplifying NIRF signals prior to integration with a CCD chip. Due to the fast response time of the photocathode, the photocathode of the image intensifier can additionally be modulated at high radiofrequencies, for example 100 MHz, for conducting FD measurements for NIRF tomography of interior tissues contrasted by NIRF imaging agents [13, 14]. In order to recover the AC amplitude and phase delay of NIRF signals for tomography, the phase of the intensifier modulation is evenly delayed N times (typically N = 32 or 64) between 0 and 360 degrees relative to the phase of the laser diode modulation. In this case, a series of phase-sensitive images are acquired for subsequent Fourier transformation to derive amplitude and phase. However, data acquisition and computation requires a few minutes, obviating the use of the current technology for rapid planar imaging.

Herein we developed a modulated, intensified CCD (ICCD) fluorescence imaging system for rapid planar imaging that enables electronic filtering of non-modulated ambient light that can contribute to the noise floor. The technique is rapid because it requires acquisition at only three-phase delays between the radio frequency (RF) signal driving the image intensifier and laser diode in order to extract images of AC amplitude. Herein we demonstrate this modulated planar image method to have superior TBR on a tumor mouse model expressing far-red fluorescent gene reporter, iRFP, and a mouse phantom containing NIR fluorophore, Alexa Fluor 750 (AF750), under ambient light conditions when compared to CW acquisition.

2. Materials and methods

2.1 Fluorescence imaging device using FD measurement approach

Figure 1 illustrates a schematic of the developed ICCD based NIRF FD detection system. Briefly, both the laser diode and Gen III image intensifier are RF modulated from 1 MHz to 110 MHz. The two oscillators are phase locked with a 10-MHz reference signal ensuring that they operate at the same frequency with a constant phase difference. For far-red iRFP imaging, the modulated laser light operating at 690 nm wavelength (HPD 1305-9mm-69005, Intense, NJ, USA) is first delivered by an optical fiber, and then filtered by a "clean up" filter (690FS10-25, Andover, NH, USA) for removing undesirable side band components, and finally expanded by a diffuser to illuminate the object laid on the stage with a field of view (FOV) of radius 5 cm. The fluorescence collection is implemented through two emission filters (720FS10, Andover, NH, USA) separated by a focus lens to increase the optical density at the excitation light wavelength and improve the measurement sensitivity. For NIRF imaging, the corresponding laser diode and filters were replaced with a 785 nm laser diode (HPD 1005-9mm-78503 model, Intense, North Brunswick, NJ), a "clean up" filter (LD01-785/10, Semrock, NY, USA) and two 830 nm band pass emission filters (830FS10, Andover, NH, USA). Finally, the filtered fluorescence signals are recorded with a modulated ICCD camera at an introduced phase delay η. The whole imaging process is controlled by a custom LabVIEW based interface (National Instruments, Austin, TX). For continuous wave imaging, no RF signals were used to modulate the intensifier photocathode and laser diode.

2.2 Three-phase delay technique for recovering AC amplitude

In order to understand how three-phase delays can be used to accurately collect planar images of AC amplitude, it is appropriate to review the homodyne detection scheme. As intensity-modulated fluorescent light is generated and propagates through the high scattering tissue, it becomes amplitude attenuated and phase-shifted relative to the incident-modulated excitation light. The attenuation and phase-shift arises from quantum efficiency and lifetime of the fluorophore, and the absorption and scattering properties of the intervening tissue [15]. Suppose the emitted light $L(x, y)$ from the tissue or phantom surface that reaches the

#200854 - $15.00 USD Received 6 Nov 2013; revised 22 Jan 2014; accepted 22 Jan 2014; published 24 Jan 2014

photocathode of the image intensifier has a phase delay, $\theta(x,y)$; average intensity, $L_{DC}(x,y)$; and amplitude intensity $L_{AC}(x,y)$ at the modulation frequency ω:

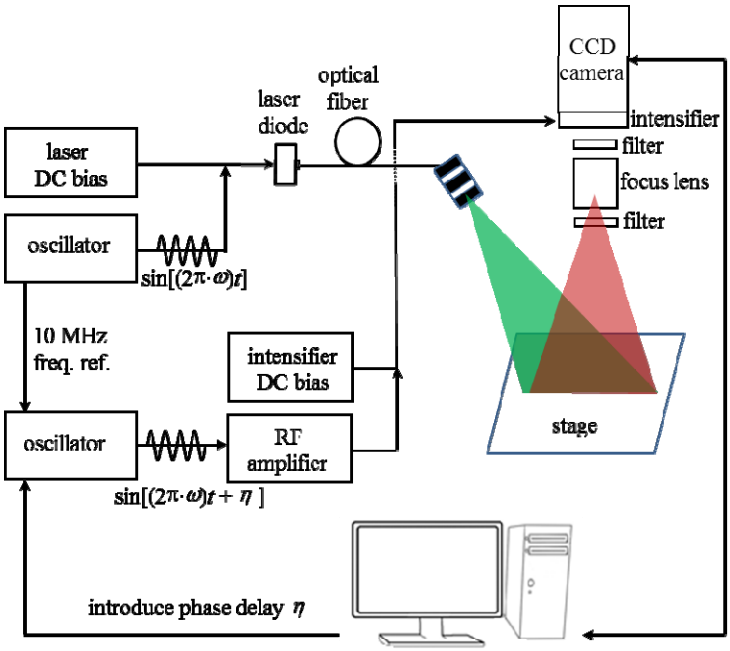

Fig. 1. Schematic of fluorescence imaging device using a modulated ICCD camera and laser diode.

$$L(x,y) = L_{DC}(x,y) + L_{AC}(x,y)\cos\left[\omega t + \theta(x,y)\right] \tag{1}$$

The modulated gain of the image intensifier is comprised of DC and AC components denoted by G_{DC} and G_{AC}, respectively, and an additional phase delay θ_{inst} owing to the instrument response time at the modulation frequency:

$$G = G_{DC} + G_{AC}\cos(\omega t + \theta_{inst}) \tag{2}$$

The resulting signals prior to striking the phosphor screen is a product of $L(x,y)$ and G, which contains both high frequency and low frequency signals:

$$\begin{aligned} S(x,y) = L(x,y)\times G = {} & L_{DC}(x,y)\cdot G_{DC} + L_{DC}(x,y)\cdot G_{AC}\cos[\omega t + \theta_{instr} + \eta] \\ & + G_{DC}\cdot L_{AC}(x,y)\cos\left[\omega t + \theta(x,y)\right] \\ & + \frac{L_{AC}(x,y)G_{AC}}{2}\cos(-\theta(x,y) + \theta_{inst} + \eta) \\ & + \frac{L_{AC}(x,y)\cdot G_{AC}}{2}\cos\left[2\omega t + \theta_{inst} + \theta(x,y)\right] \end{aligned} \tag{3}$$

Since the response time of the phosphor screen is sub-milliseconds (ms), the high frequency signals are automatically filtered out and the low frequency signals registered on the CCD camera are simply:

$$S(x,y) = DC(x,y) + AC(x,y)\cos(-\theta(x,y) + \theta_{inst} + \eta) \tag{4}$$

#200854 - $15.00 USD Received 6 Nov 2013; revised 22 Jan 2014; accepted 22 Jan 2014; published 24 Jan 2014

Where $DC(x,y) = L_{DC}(x,y) \cdot G_{DC}$, $AC(x,y) = \frac{L_{AC}(x,y)G_{AC}}{2}$, and η is the phase lag between the modulation of the laser diode and the image intensifier.

If triple images denoted as $S_0 = S\left(x,y,\eta = 0^0\right)$, $S_{90} = S\left(x,y,\eta = 90^0\right)$, and $S_{180} = S\left(x,y,\eta = 180^0\right)$ with a 90 degree phase-shift between acquired, sequential images, then the relative $AC(x,y)$ amplitude of detected signals can be recovered using the following equation:

$$AC(x,y) = \frac{1}{2}\sqrt{\left(2S_{90} - S_0 - S_{180}\right)^2 + \left(S_{180} - S_0\right)^2} \tag{5}$$

2.3 Spectral characterization of ambient light

The spectrum of the ambient light was assessed using a spectrometer (USB4000, Ocean Optics, Dunedin, FL). This was done by directing the spectrometer's input toward each light source in the room including the fluorescent room lights, the overhead surgical lights, and the surgeon's head lamp.

2.4 Modulation depth

To verify the sinusoidal variation of the detected signals predicted by Eq. (4) and to determine the modulation depth, $M = AC/DC$, a white paper was placed on the stage and the backscattered excitation light was collected using a neutral density filter. A series of 32 phase-sensitive images were acquired at different modulation frequencies and the amplitude modulation was computed from the fast Fourier transform (FFT) as previously described [16]. Because the collected signal acquired with intensifier modulation is smaller when compared to that without intensifier modulation, the signal-to-noise ratio (SNR) of AC images can be expected to be less than that of DC images. As the instrument response is the function of the modulation frequency, we sought to determine the optimal modulation frequency for the greatest SNR while still allowing improved contrast from ambient light rejection not directly possible from DC images.

2.5 Mouse model and far-red fluorescence imaging

Orthotopically implanted breast cancer MDA-MB-231 cell (1.0×10^6) expressing iRFP gene reporter into the lower right mammary fat pad of Nu/Nu female mice were imaged using the CW and FD acquisition at 10 weeks of age. iRFP gene reporter has excitation and emission maxima located at the far-red window (690/710 ex/em), whose fluorescence can be enhanced by a heme catabolism product called biliverdin existing in all animals [17]. To reduce food background fluorescence, the mice were fed AIN-93G (OpenSource Diets, New Brunswick, NJ, USA). iRFP fluorescence imaging was performed on mice two weeks after implantation of the transfected breast cancer cells with the fluorescent room lights on. The integration time of ICCD camera operated in both CW and FD modes was set to 33 ms. All experiments were carried out according to protocols approved by the institutional Animal Welfare Committee and in compliance with the American Association for Laboratory Animal Care.

2.6 Fluorescent mouse shaped phantom and NIRF imaging

To mimic NIRF fluorescence imaging under ambient light conditions, we employed a fluorescent mouse-shaped phantom (Caliper, Hopkinton, MA). The mouse shaped phantom was made of polyurethane containing scattering particles to mimic the tissue scattering and contained a fluorescent target consisting of plastic tubing containing a 31.4 μM solution of AF750 fluorophore in a 19 μL volume placed on the ventral side of mouse phantom. To mimic the "in-band" contributions from sources in the operating room, an 830 nm laser diode (DL5032-001, Thorlabs, Newton, NJ) operating in CW mode illuminated the field of view with incident power of around 3.0 $\mu W/cm^2$. NIRF imaging was performed on the mouse

#200854 - $15.00 USD Received 6 Nov 2013; revised 22 Jan 2014; accepted 22 Jan 2014; published 24 Jan 2014

phantom illuminated with the 830 nm laser diode and the integration time of the ICCD operated in both CW and FD modes was set to 33 ms. To determine the limit in the ratio between fluorescence signal and ambient light, we increased the power of the incident power of 830 nm laser diode up to 146 μW/cm^2 and assessed its impact on target-to-background ratio (TBR) as described below.

2.7 Image analysis by figures of merit

To assess the TBR the target signal was selected over the region of interest (ROI) encompassing the implanted iRFP tumor or the rod tip containing AF750 fluorophore and the background signal was selected to be the contralateral region of the same area. The TBR can be computed by [18]:

$$TBR = \frac{P^T}{P^B} \tag{6}$$

where P^T and P^B represent the mean intensify from the target and background ROIs, respectively, and the SNR in decibels (dB) was calculated as:

$$SNR = 20\log_{10}\frac{P^T - P^B}{\sigma} \tag{7}$$

where σ was the standard deviation of intensity over the background ROI.

3. Results

3.1 Modulation depth as a function of modulation frequency

Figure 2(a) shows that the phase-sensitive intensities of a randomly chosen pixel on the acquired image vary sinusoidally for three representative modulation frequencies (1MHz, 50MHz, and 100 MHz), consistent with that predicted by Eq. (4). The calculated modulation depths (M) under varying modulation frequencies are shown in Fig. 2(b). In most cases, the modulation depth is more than 0.3, with the exception of modulation frequency ≥110 MHz, indicating the limit of FD instrument response. The maximum modulation depth was obtained at 50 MHz modulation frequency. Hence, we set the modulation frequency to 50 MHz for the following studies.

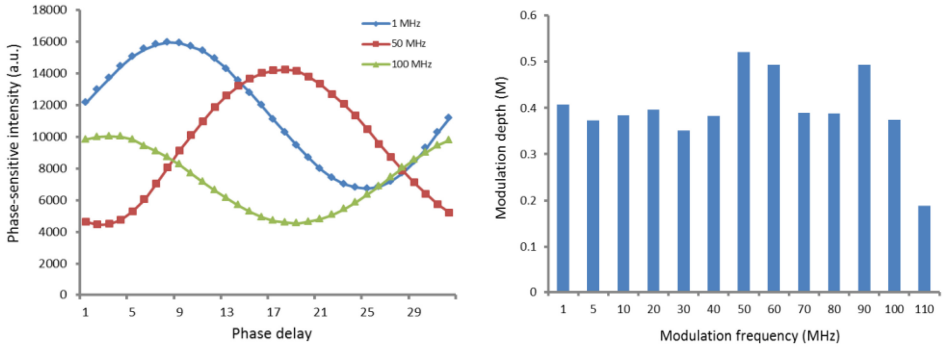

(a) (b)

Fig. 2. (a) Data depicting the sinusoidal variation of detected phase-sensitive intensity for a randomly chosen pixel at three representative modulation frequencies, where a.u. represents the arbitrary unit. (b) Modulation depth (M) at various modulation frequencies.

#200854 - $15.00 USD Received 6 Nov 2013; revised 22 Jan 2014; accepted 22 Jan 2014; published 24 Jan 2014

3.2 Far-red fluorescence imaging

Figure 3 (a)-3(c) show the acquired iRFP fluorescence images at the phase delays of 0°, 90° and 180°, respectively, under ambient light conditions. The AC amplitude image computed by their combination using the relationship in Eq. (5) is shown in Fig. 3(d). The DC intensity acquired using CW acquisition is shown in Fig. 3(e). We can observe that DC image is strongly contaminated by the fluorescent room lights in our laboratory as might be expected in the surgical suite, whose spectra is shown in Fig. 3(f) with a peak within the "in-band" wavelengths used in far-red fluorescence imaging. In comparison, the AC amplitude image is tolerant to the fluorescent room lights.

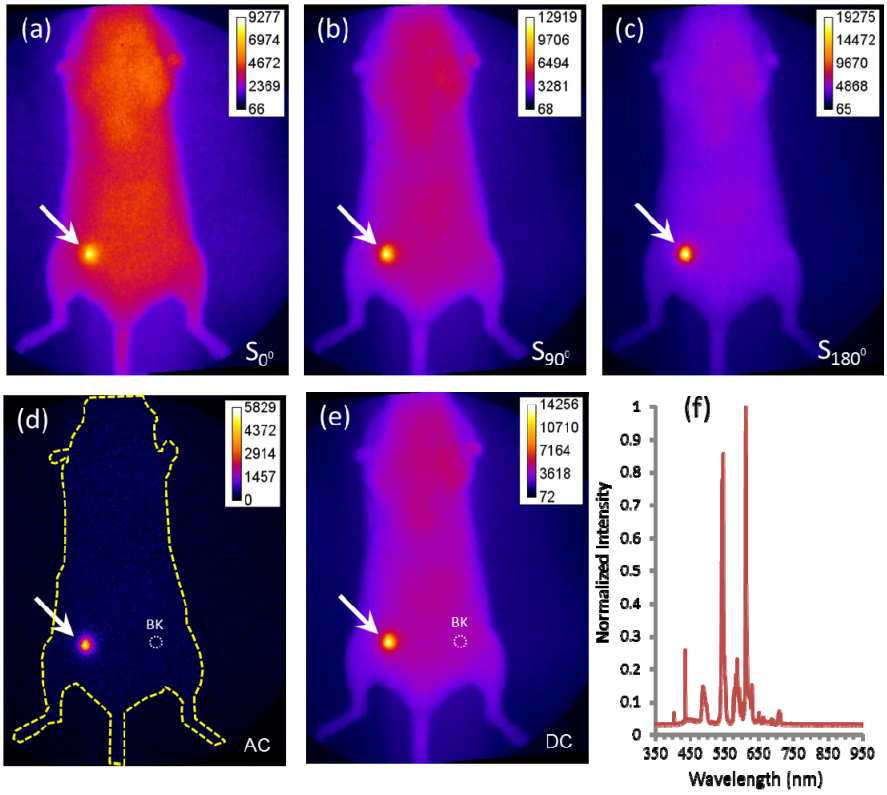

Fig. 3. iRFP fluorescence images acquired at the phase delay (a) 0°, (b) 90° and (c) 180° from a representative mouse. (d) The extracted image of AC amplitude. (e) CW Image of DC. (f) Spectra of the fluorescent room lights acquired in the surgical suite showing far red spectral. The arrows point to the breast cancer location and the dashed circles represent the background (BK) ROIs.

To calculate the TBR and SNR, the dashed circles in Fig. 3(d) and 3(e) represent the chosen background ROIs and the target ROIs were chosen to encompass the breast tumor pointed by the arrows. Table 1 lists the P^T, P^B, σ, TBR and SNR of AC amplitude and DC intensity images from the mouse depicted in Fig. 3 and Table 2 lists the cumulative TBR and SNR of AC amplitude and DC intensity images in five mice similarly imaged. The TBR from AC amplitude image is more than 5 times greater than that from the DC intensity image. The statistical analysis shows a significant difference in the TBR predicted from the AC amplitude and DC intensity images (paired t-test with $\alpha = 0.05$).

#200854 - $15.00 USD Received 6 Nov 2013; revised 22 Jan 2014; accepted 22 Jan 2014; published 24 Jan 2014

Table 1. Comparison of the P^T, P^B, σ, TBR and SNR of AC amplitude and DC intensity in mouse depicted in Fig. 3, where a.u. represents arbitrary unit.

Images	P^T (a.u.)	P^B (a.u.)	σ	TBR	SNR (dB)
AC amplitude	3708	255	126	14.5	28.7
DC intensity	11438	4262	139	2.7	34.3

Table 2. Comparison of TBR and SNR of AC amplitude and DC intensity in five mice

Figures of Merit	AC amplitude	DC intensity
Target-to-background ratio TBR	13.6 ± 4.7	2.5 ± 0.4
Signal-to-background ratio SNR	27.0 ± 3.2	32.9 ± 3.4

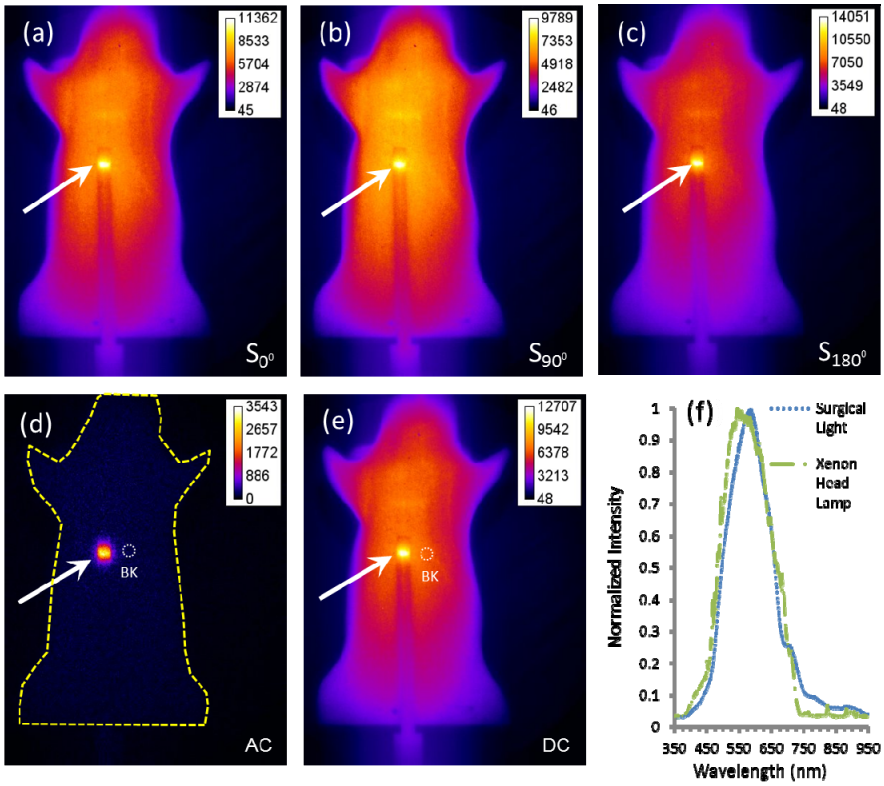

Fig. 4. NIRF images acquired at the phase delay (a) 0°, (b) 90° and (c) 180° from a mouse-shaped phantom. (d) The extracted image of AC amplitude. (e) CW image of DC. (f) Spectra of the surgical lights and the surgeon's head lamp in the operating room showing interference in the NIR wavelength region. The arrows point to the rod tips containing AF750 fluorophore and the dashed circles represent the background (BK) ROIs.

3.3 NIRF imaging

Figure 4 (a)-4(c) show the NIRF images acquired at the phase delays of 0°, 90° and 180°, respectively, in the phantom with a target containing NIRF dye, AF750. The AC amplitude image is shown in Fig. 4(d) and the DC intensity image acquired in CW mode is shown in Fig. 4(e). Similar to the far-red fluorescence imaging, the DC image is strongly contaminated by the ambient light. In comparison, the recovered AC amplitude is insensitive to the ambient

#200854 - $15.00 USD Received 6 Nov 2013; revised 22 Jan 2014; accepted 22 Jan 2014; published 24 Jan 2014

light. Figure 4(f) shows the measured spectra of the surgical light and xenon head lamp in the operating room in the MD Anderson Cancer Center, containing the spectra located within "in-band" of NIRF collection filters. Because our laboratory fluorescent lighting did not have a near-infrared spectral component as the overhead surgical light and xenon head lamp, we simulated ambient light in the surgical suite with 3 $\mu W/cm^2$ CW illumination from an 830 nm laser diode. While the spectral power of surgical lighting and head lamps can vary, we found that our approach can effectively improve contrast even with 80 $\mu W/cm^2$ 830 nm light.

In order to assess the TBR and SNR, the dashed circles in Fig. 4(d) and 4(e) represent the chosen background ROIs and the target ROIs were chosen to encompass the rod tips containing AF750 fluorophore pointed by the arrows. Table 3 lists the P^T, P^B, σ, TBR, and SNR of AC amplitude and DC intensity images of the mouse-shaped phantom depicted in Fig. 4. The TBR from AC amplitude image is more than 10 times higher than that from DC intensity image. In addition, the AC amplitude image has the similar SNR as that of DC image. Because there are no fluorescent gene reporters excitable in the NIR wavelength regime to conduct studies similarly to those in Fig. 3 and Tables 1 and 2, we employ the phantom to compare the NIRF AC amplitude and DC intensity imaging. The NIRF phantom imaging data was replicated and no differences in SNR and TBR were found.

Table 3. Comparison of the P^T, P^B, σ, **TBR and SNR of AC amplitude and DC intensity in mouse-shaped phantom depicted in Fig. 4, where a.u. represents arbitrary unit.**

Images	P^T (a.u.)	P^B (a.u.)	σ	TBR	SNR (dB)
AC amplitude	2833	152	85	18.6	30
DC intensity	11656	6632	143	1.8	30.9

As we increased the incident power of 830 nm CW illumination from 3.0 $\mu W/cm^2$ to 146 $\mu W/cm^2$, the TBR decreased as expected. In the absence of CW illumination, the signal from the fluorescent target was measured to be an average 0.88 $\mu W/cm^2$. Assuming a TBR value of 1.86 is chosen as the minimum image contrast used for tumor margin identification [19], then we determined that a maximum power of incident 830 nm CW illumination that could delineate the fluorescent target was 80.88 $\mu W/cm^2$. Using these numbers, we estimate that for our current imaging system, the limit of the ratio between the fluorescence signal and the ambient light leakage that would permit fluorescence detection is 1/92.

4. Discussion

In general, diffuse (non-fluorescence) or fluorescence-enhanced optical imaging is performed using one of the three measurement approaches: (i) the CW domain, (ii) the TD domian, and (iii) the FD. In a CW-based measurement approach, the incident excitation energy from a source is constant over timescale of milliseconds or modulated at low frequency (a few kHz) and the re-emitted fluorescence energy from exogenous agents is likewise constant. In a TD based measurement approach, ultrafast (with duration range from femtosecond to picosecond) laser pulses are employed to illuminate the tissue and the generated fluorescent signals are detected by a streak camera, time-gated CCD camera or time-correlated single photon counting device. When a light pulse is launched onto the tissue, its profile will be broadened with pico- to nano- second "time-of-flight". The generated fluorescence pulse is further broadened owing to the lifetime of the fluorophore and its propagation within the scattering tissue. In comparison to the CW-based approach, the TD approach is capable of discriminating the fluorescence decay kinetics from changes in fluorophore concentration. On the downside, the SNR of TD approach suffers significantly and the cost and complexity of the instrumentation is relatively high. FD approach is directly related TD approach through the Fourier transform. The FD-based instrumentation can be operated in a non-light-tight environment due to the fact that the amplitude of the detected fluorescence is insensitive to the ambient light. In addition, FD approach has an added advantage of considerably high SNR with respect to TD approach, due to steady-state measurements of a time-dependent light propagation process.

#200854 - $15.00 USD Received 6 Nov 2013; revised 22 Jan 2014; accepted 22 Jan 2014; published 24 Jan 2014

Sexton, et al. [10] have also used a Gen II intensifier coupled to a CCD to demonstrate a simple scheme to filter ambient light for greater contrast arising from protoporphyrin IX following visible light excitation. In their work, they collect remitted light with repetitive 500 μs exposures alternating with on-off LED excitation illumination to enable real-time subtraction to enhance contrast. Because the long microsecond ICCD integration time captures all "photon time-of-flights," the technique is not representative of TD approaches, but rather is essentially similar to acquiring a CW image with excitation illumination and subtracting a second CW image acquired without excitation illumination. Their work shows the elimination of ambient light improves contrast over a commercial surgical microscope.

If the goal of cancer imaging is to detect cancer cells in the body, then the achievable tumor-to-background ratio (or contrast) should be as high as possible using advanced measurement strategies. Far-red fluorescence imaging involves in the implantation of cancer cells expressing iRFP or IFP1.4 protein into small animals orthotopically to monitor tumor growth and metastasis. NIRF molecular imaging involves the administration of a targeted-agent labeled with a fluorophore that has both excitation and emission maxima within a "NIR" window (>780 nm) for fluorescence-guided surgery. In the operating room, the overhead surgical lights and surgeon's head lamp as well as the fluorescent room lights can "leak" through filters and reduce the TBR that is necessary for visual delineation of tumor. In this study, we demonstrated that the extracted AC amplitude images from both far-red fluorescence and NIRF imaging systems using a modulated ICCD camera and laser diode are insensitive to the ambient light with higher TBR and reasonable SNR compared with the CW measurement approach. Due to the higher TBR, the AC amplitude image will be presented to the surgeon for determination of tumor margin with high accuracy. With this approach, the AC amplitude image can be recovered through a three-phase delay technique while the integration time of ICCD camera is 33 ms with a total length of less than 100 ms. By increasing the gain of the intensifier, we have further demonstrated that the integration time of ICCD camera can be further reduced to less than 10 ms without damage to the intensifier. In this case, the total time required for data acquisition and computation can be reduced largely, making real-time intraoperative NIRF-guided tumor detection possible. Previously, we showed that NIRF labeled antibody can accurately target the tumor in a prostate cancer mouse model using the CW based ICCD imager in a dark room [1]. For translation into the operating suite, we seek to employ the developed NIRF FD imaging system to maximize contrast under ambient light conditions.

There are limitations to the current study. Because we sought to characterize the performance of AC amplitude over DC intensity imaging, we did not include an exogenous, molecularly targeting imaging agent, since contrast would be influenced not only by the ICCD operation, but also by the performance of the molecular imaging agent to partition to the target region and clear from the normal tissues. By using the far-red gene reporter, we explored the camera performance independent of an imperfectly targeted exogenous imaging agent. Because there are no NIRF fluorescent gene reporters, we used the phantom to explore performance of AC amplitude and DC intensity imaging. For implementation in the surgical suite, the imaging performance will depend upon both the device as well as the imaging agent. The selective molecular targeting of the imaging agent and the depth of the targeted tissue will inevitably impact the amount of fluorescence that can be collected by the ICCD system. However, because the camera system is operated in homodyne mode, the exposure times of the camera can also be lengthened to acquire sufficient SNR to detect contrast, albeit at increased imaging time. In the past, we have conducted DC intensity imaging of exogenous NIRF molecular imaging agents in animals and of trace doses of ICG in humans in the surgical suite [20]. Because our results show the superiority of AC amplitude imaging over DC intensity imaging, we expect AC amplitude imaging will improve imaging contrast. However, we do acknowledge that there is ultimately a lower limit to the ratio of fluorescent light and ambient light that can enable contrast with sufficient SNR. Our continuing work is to identify the ICCD camera parameters to assure efficient translation into a well-lit surgical suite.

#200854 - $15.00 USD Received 6 Nov 2013; revised 22 Jan 2014; accepted 22 Jan 2014; published 24 Jan 2014

Acknowledgments

We thank Grace Wu for the iRFP cells and Holly Robinson for preparation of the breast cancer mouse model. The work is supported in part by U54 CA136404 and R01 CA128919.

#200854 - $15.00 USD Received 6 Nov 2013; revised 22 Jan 2014; accepted 22 Jan 2014; published 24 Jan 2014